SPECT3D – A Multi-Dimensional Collisional-Radiative Code for Generating Diagnostic Signatures Based on Hydrodynamics and PIC Simulation Output

J. J. MacFarlane*, I. E. Golovkin, P. Wang, P. R. Woodruff, and N. A. Pereyra

Prism Computational Sciences
455 Science Drive, Suite 140
Madison, WI 53711

*corresponding author
Email: jjm@prism-cs.com

Published in:
High Energy Density Physics, Vol. 3, p. 181-190 (2007).

Abstract

SPECT3D is a multi-dimensional collisional-radiative code used to post-process the output from radiation-hydrodynamics (RH) and particle-in-cell (PIC) codes to generate diagnostic signatures (*e.g.*, images, spectra) that can be compared directly with experimental measurements. This ability to post-process simulation code output plays a pivotal role in assessing the reliability of RH and PIC simulation codes and their physics models. SPECT3D has the capability to operate on plasmas in 1-D, 2-D, and 3-D geometries. It computes a variety of diagnostic signatures that can be compared with experimental measurements, including: time-resolved and time-integrated spectra, space-resolved spectra and streaked spectra; filtered and monochromatic images; and x-ray diode signals. Simulated images and spectra can include the effects of backlighters, as well as the effects of instrumental broadening and time-gating. SPECT3D also includes a drilldown capability that shows where frequency-dependent radiation is emitted and absorbed as it propagates through the plasma towards the detector, thereby providing insights on where the radiation seen by a detector originates within the plasma.

SPECT3D has the capability to model a variety of complex atomic and radiative processes that affect the radiation seen by imaging and spectral detectors in high energy density physics (HEDP) experiments. LTE (local thermodynamic equilibrium) or non-LTE atomic level populations can be computed for plasmas. Photoabsorption rates can be computed using either escape probability models or, for selected 1-D and 2-D geometries, multi-angle radiative transfer models. The effects of non-thermal (*i.e.*, non-Maxwellian) electron distributions can also be included. To study the influence of energetic particles on spectra and images recorded in intense short-pulse laser experiments, the effects of both relativistic electrons and energetic proton beams can be simulated.

SPECT3D is a user-friendly software package that runs on Windows, Linux, and Mac platforms. A parallel version of SPECT3D is supported for Linux clusters for large-scale calculations. We will discuss the major features of SPECT3D, and present example results from simulations and comparisons with experimental data.

Keywords: Atomic kinetics, collisional-radiative modeling, radiation transport, atomic kinetics, laser-produced plasmas, z-pinch plasmas, high energy density physics.

INTRODUCTION

Radiation-hydrodynamics (RH) and particle-in-cell (PIC) codes are commonly used to simulate the heating and evolution of plasmas in a wide variety of high energy density physics (HEDP) experiments, including laser-driven inertial fusion [1], z-pinch [2,3], short-pulse laser [4,5], and commercially-driven plasma radiation source [6] experiments. A critical aspect of assessing the reliability of such simulation codes is the ability to compare simulation results directly with experimental measurements, such as high-resolution spectra, images, or x-ray diode (XRD) signals. To generate diagnostic signatures based on simulation code output, a "post-processing" code is typically employed to compute the spectral intensity at virtual detectors placed at the location of diagnostic instruments. The radiative properties of HEDP plasmas are often complicated by the fact that they deviate from local thermodynamic equilibrium (LTE). In particular, atomic level populations can be affected by the non-local nature of radiation fields (through photoionization and photoexcitation), and by the effects of non-thermal energetic electrons and protons (as in the case of short-pulse laser experiments). Because of this, it is important that the post-processing code be able to model the complex atomic and radiative processes that affect the radiation seen by imaging and spectral detectors in HEDP experiments.

SPECT3D is a multi-dimensional collisional-radiative code used to post-process the output from radiation-hydrodynamics and particle-in-cell codes. By computing diagnostic signatures that can be compared with experimental measurements, it plays an essential role in assessing the reliability of RH and PIC simulation code results. It computes a variety of results at virtual detectors placed at user-specified locations. Simulated diagnostic signals include: time-resolved and time-integrated spectra, 1-D space-resolved spectra, and streaked spectra; filtered and monochromatic images; filtered XRD signals, and absolutely calibrated fluxes at a detector. Simulated images and spectra can include the effects of continuum or narrow-band backlighters. Instrumental effects such as the spectral resolution of spectrometers, spatial smoothing of images, and time-gating can be included. Signals can be computed using several viewing geometries, including orthographic and point projection, as well as that for a spherical crystal-backlighter imaging system. SPECT3D also includes a "drilldown" capability (*i.e.*, the

display of depth-dependent properties along a particular line-of-sight through the plasma) that shows where frequency-dependent radiation is emitted and absorbed as it propagates through the plasma towards the detector. This feature is particularly useful in providing insights as to where the radiation seen by a detector originates within the plasma.

SPECT3D is currently being used to post-process output from a variety of 1-D, 2-D, and 3-D RH codes, including ALEGRA [7], DRACO [8], CTH [9], and HELIOS-CR [10]. In addition, SPECT3D has recently been upgraded to post-process LSP [11,12] PIC simulation results. To study the influence of energetic particles on spectra and images recorded in short-pulse laser experiments, SPECT3D has been updated to include the effects of both relativistic electrons and energetic proton beams. Energetic particle distributions are obtained from LSP PIC code output, and their effects are included in computing non-LTE atomic level populations, emergent spectra, and images, thereby allowing the study of diagnostic signatures arising from energetic particles.

In this paper, we describe the major features of SPECT3D, and present some sample results. A description of the atomic physics database used by SPECT3D is provided in an appendix at the end of this paper.

MAJOR FEATURES OF SPECT3D

The primary function of SPECT3D is to generate simulated images and spectra, based on RH and PIC code simulation code output, which can be directly compared with experimental measurements. This serves to test the reliability of the physics modeling in the RH or PIC simulation codes. Alternatively, SPECT3D can be applied to plasma grids generated with a supporting application, PLASMAGEN, which generates 1-D and 2-D multi-material plasma grids with user-specified temperature and density distributions. This approach is often useful in trying to gain insights into the sensitivity of spectra and images to changes in plasma conditions. While SPECT3D can be set up to run calculations for simple single-cell plasmas with a specified uniform temperature and density, its primary purpose is to calculate

the radiative properties of spatially distributed plasmas. The separate code, PrismSPECT [13], has been developed to more conveniently study the radiative properties of single-cell plasmas.

In a SPECT3D simulation, the radiation incident at a detector is computed by solving the radiative transfer equation along a series of lines-of-sight (LOSs) through the plasma grid. At each plasma volume element along the LOS, the frequency-dependent absorption and emissivity of the plasma is computed. In determining the emission and absorption of materials, SPECT3D models materials in two ways. The more common approach is to use detailed configuration (or energy level) accounting (DCA), in which a material is composed of one or more atomic elements, with the atomic levels of each element being explicitly modeled in the calculation. For DCA materials, LTE or non-LTE atomic level populations are computed, and the plasma absorption and emissivity are determined from the atomic level populations. The second approach for modeling the frequency-dependent radiative properties of materials is to perform table look-up of opacities and emissivities from pre-computed multi-frequency tables (such as those used by RH codes). Pre-computed tables can be generated for plasmas under the assumption of LTE, in which case their radiative properties are a function of only the local temperature and density. SPECT3D supports the use of PROPACEOS [14] multi-frequency opacity tables.

For DCA materials, steady-state atomic level populations, and the corresponding images and spectra resulting from them, can be computed at multiple (independent) simulation times corresponding to the output from the RH codes. Alternatively, atomic level populations can be computed from the solution of time-dependent atomic rate equations, in which case the time-dependent plasma conditions from the RH and PIC codes are utilized.

SPECT3D has been designed to be both easy to use and flexible. It utilizes cross-platform user-interface and graphics software. Results from SPECT3D simulations are conveniently displayed using the SPECT3D VISUALIZER graphics application. Atomic models – *i.e.,* a selected set of atomic energy levels and a specification of how the levels are split (*e.g.,* configuration averaged, L-S term split, or fine structure split) – can be chosen from a collection of preconfigured models, or users can generate their own customized atomic models. To facilitate the generation of custom atomic models, the

AtomicModelBuilder application was developed to conveniently select energy levels from the atomic physics database and specify the degree of level splitting.

Plasma and Detector Geometries

SPECT3D supports a variety of plasma geometries, including: 1-D planar, cylindrical, and spherical; 2-D Cartesian and cylindrical *r*-*z*; and 3-D Cartesian. For plasmas that have one or more dimensions of infinite extent (*e.g.*, the *z* dimension for a 2-D Cartesian *x*-*y* grid), the plasma in the SPECT3D simulation is clipped to a specified length to give the plasma volume a finite size. In cases where RH simulations are performed using periodic boundary conditions, such as pie slices in 2-D Cartesian *x*-*y* geometry which are repeated about the *z*-axis, SPECT3D computes images and spectra for the entire (replicated) plasma.

For a given plasma distribution and detector setup (*i.e.*, detector location, size, and shape), the radiation at the detector plane can be computed using orthographic projection or point projection viewing geometries. Figure 1 shows a schematic illustration of orthographic and point projection viewing models. The detector is divided into a grid of pixels in the horizontal and vertical directions for a rectangular detector, and in the radial and azimuthal directions for a disk detector. For orthographic projection, the rays shooting through the plasma from each detector pixel are parallel. For point projection, the rays from each detector pixel are directed at the backlighter position. Point projection viewing is typically used in cases where small backlighter sources are utilized. In the case of orthographic projection, the backlighter has an extended size that is equal to the size of the detector. Regardless of viewing geometry, the coordinate system of the target-plasma-backlighter system is defined to be that of the plasma coordinate system, which is defined by the RH or PIC code.

A spherical crystal viewing geometry is a special case for simulating backlit images using a monochromatic backlighter (see Figure 2). In this case, the backlighter sits on the Rowland circle. Photons from the backlighter pass through the plasma and reflect off a spherical crystal. The reflected rays are imaged on the virtual detector plane. Fig. 2 shows how lines of sight that originate from different parts of the detector reflect off the spherical crystal and move through the plasma to the backlighter.

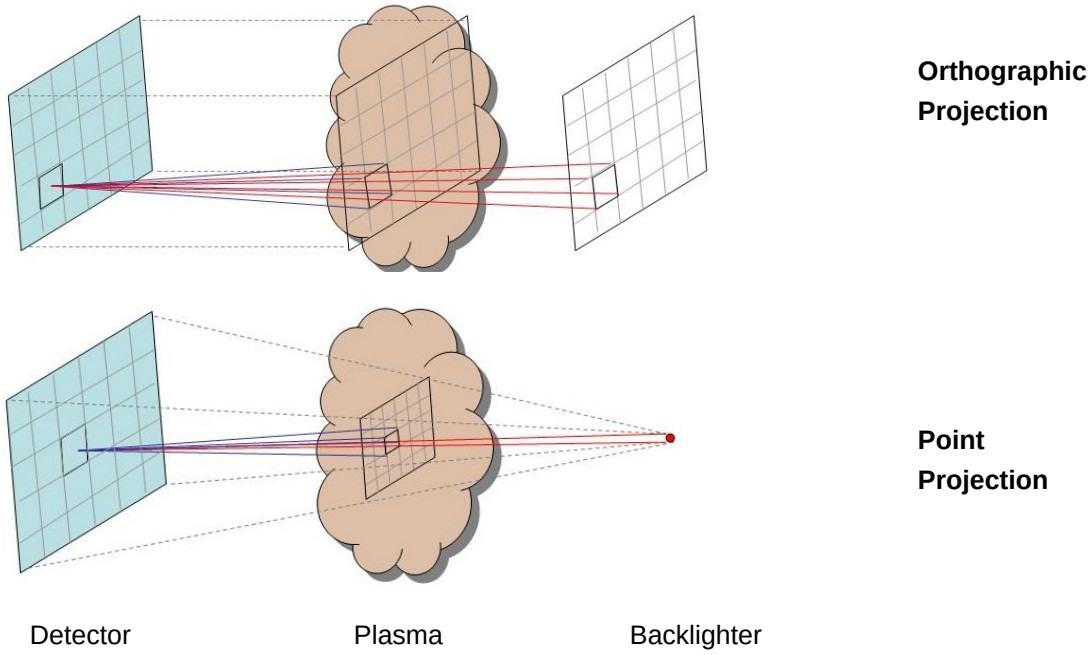

Figure 1. Schematic illustration of orthographic projections and point projection viewing models for a rectangular virtual detector in SPECT3D. The solid lines indicate solid angle to the plasma and backlighter as viewed at a detector pixel.

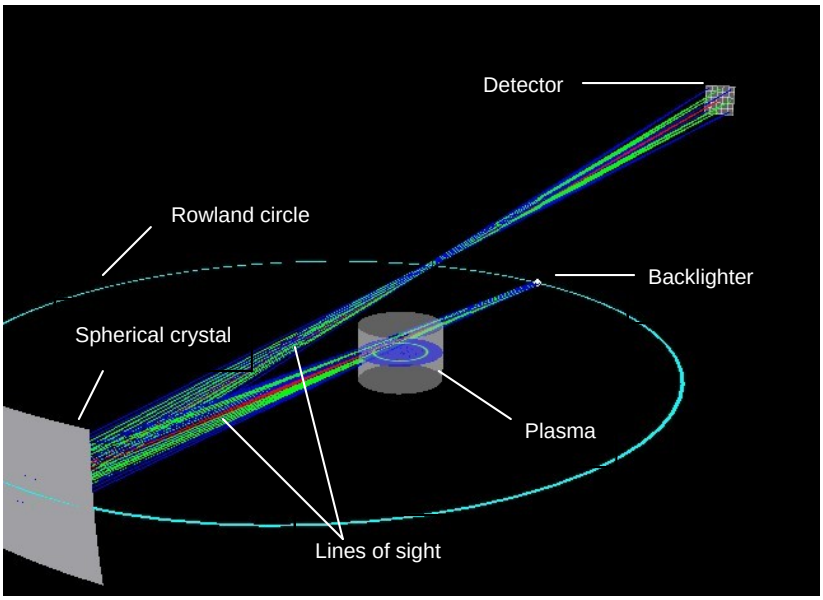

Figure 2. Schematic illustration of spherical crystal viewing model. The backlighter resides on the Roland circle. Photons from the backlighter propagate through the plasma, reflect off the spherical crystal, and are recorded at the detector. Lines-of-sight originating from different points on the detector plane (center, sides, and corners) are shown as lines of different shades.

Backlighter Models

Two types of backlighter spatial intensity profiles are supported in SPECT3D: uniform and distributed. For a uniform backlighter, the intensity originating from the backlighter is assumed to be spatially uniform, and the specific intensity is computed along a single line of sight from the backlighter to each pixel in the detector plane. For a uniform backlighter, the size of the backlighter is used in computing the total flux seen at the detector.

For a backlighter with a distributed spatial profile, the intensity emitted from the backlighter is given by:

$$I(r) = I_0 \exp[-(r / r_0)^n] \tag{1}$$

where I_0 is the intensity at the center of the backlighter spot, *r* is the radial distance from the center of the spot, and r_0 and *n* are user-specified constants. For backlighters with distributed spatial profiles, the backlighter is broken up into a grid of points, each of which casts a line of sight to each pixel in the detector plane.

The frequency dependence of the backlighter can be modeled using several approaches: narrow band backlighters, such as those originating from a single strong emission line; continuum backlighters modeled using a Planckian spectrum; and a hybrid narrow band-continuum source. In addition, the backlighter intensity spectrum can also be modeled with a user-provided data file.

Radiative Transfer and Flux at the Detector

The specific intensity, I_ν^{Det}, at a detector pixel is computed along each line of sight by solving the integral form of the radiative transfer equation [15]:

$$I_\nu^{Det} = I_\nu^{BL} e^{-\tau_{Max}} + \int_0^{\tau_{Max}} S_\nu \; e^{-\tau_\nu} \, d\tau_\nu \tag{2}$$

where

$$S_\nu = \eta_\nu / (\kappa_\nu + \sigma_\nu) \quad , \tag{3}$$

$$\tau_\nu(z) = \int_0^z \kappa_\nu \, dz \quad , \tag{4}$$

η_ν is the plasma emissivity at frequency ν, κ_ν is the absorption coefficient, σ_ν is the scattering coefficient, $\tau_\nu(z)$ is the optical depth as measured to a position z along the line of sight relative to the detector, τ_{Max} is the total optical depth along the line of sight, and I_ν^{BL} is the specific intensity at the back boundary of the plasma (defined by the backlighter intensity).

The total flux at the detector, F_ν, is given by summing over lines of sight, ℓ:

$$F_\nu = \sum_\ell^{N_{LOS}} F_\nu^{\ell} \tag{5}$$

where

$$F_\nu^{\ell} = I_{\nu,\ell}^{P} \, \Delta\Omega_P^{\ell} + I_{\nu,\ell}^{BL} \, e^{-\tau_{\max}} \, \Delta\Omega_{BL} \quad , \tag{6}$$

$I_\nu^P = I_{\nu,\ell}^{Det} - I_{\nu,\ell}^{BL} \, e^{-\tau_{Max}}$ is the contribution to the specific intensity at the detector that is due to the self-emission from the plasma, $\Delta\Omega_P^{\ell}$ is the solid angle of the plasma seen by the detector for line of sight ℓ, and $\Delta\Omega_{BL}$ is the solid angle of the backlighter seen by the detector.

SPECT3D generates time-resolved filtered images by computing the frequency-integrated specific intensity for each detector pixel:

$$I_\ell^{Det} = \int_{\nu_{\min}}^{\nu_{\max}} I_{\nu,\ell}^{Det} \, R_\nu \, d\nu \quad , \tag{7}$$

where $\nu_{\min}$ and $\nu_{\max}$ are the minimum and maximum photon energies, respectively, and R_ν is the frequency-dependent filter response function. Time-resolved spectra are based on the frequency-dependent *flux at the detector*. The 2-D space-integrated spectra (*i.e.*, integrated over the entire detector grid) are computed using Eq. (5). Horizontally and vertically resolved spectra are frequency-dependent spectra that are integrated in one dimension of the detector plane, but spatially resolved in the other dimension. In this case, the frequency-dependent flux at the detector per resolution element is computed.

Atomic Kinetics

For materials that use detailed configuration accounting (DCA) modeling, the populations of atomic energy levels must be computed. If designated to be in LTE, the populations are computed using the Saha equation and Boltzmann statistics [16]. For non-LTE plasmas, populations are determined from the solution of a coupled set of atomic rate equations. A description of the atomic rate equations and atomic processes included in the modeling is discussed in Ref. [10].

In SPECT3D, several options are provided for computing photoexcitation and photoionization rates. The different options involve trade-offs in CPU time and accuracy. One option for computing photoexcitation rates is based on the use of escape probabilities, where escape factors are based on fits to angle- and frequency-averaged escape probabilities for Voigt line profiles [17]. In SPECT3D, the escape probability approach is based on *local* escape factors only; that is, the radiation contributing to the photon-induced rates depends only on radiation emitted and absorbed locally within the volume element of interest. Therefore, photo-pumping due to photons originating outside of that volume element is neglected. In addition, the frequency-averaged escape probabilities consider radiation emitted and absorbed only for the transition of interest; that is, line overlap effects are not included. However, the advantage of this model is that it provides estimates of photoexcitation rates very quickly. SPECT3D also includes more accurate multi-angle radiative transfer models for computing photoexcitation and photoionization rates: one model based on long characteristics, the other based on short characteristics. In the long characteristics approach, the angle-dependent specific intensity in each volume element is computed by solving the radiative transfer equation along rays that pass through the *entire plasma grid*. By comparison, in the short characteristics approach, radiative transfer is computed along rays that are terminated at each cell boundary, with a specific intensity boundary condition that is based on interpolation (in angle space) of the specific intensities computed at the boundaries with adjacent cells [18,19]. Because of this, the short characteristic model is significantly more computationally efficient, but is somewhat less accurate. In all 1-D geometries and 2-D cylindrical *r-z* geometry, multi-angle photoexcitation and photoionization rates can be computed based on long characteristics modeling. The short characteristics option is currently implemented for 2-D cylindrical *r-z* geometry only. For other 2-D

and 3-D plasma geometries, SPECT3D currently computes photo-pumping rates using the escape probability option.

For plasmas with non-Maxwellian electron distributions, collisional excitation and ionization rates are computed by integrating the electron distribution over the electron kinetic energy. This is done using the formulation described in Ref. [20], but using cross sections described in Appendix A.

For a given population distribution, the frequency-dependent opacity and emissivity are determined by summing over the contributions of all bound-bound (*bb*), bound-free (*bf*) and free-free (*ff*) transitions using methodology described in Ref. [15].

Line profiles are modeled using a Voigt profile, and include natural (including autoionization), Doppler, and Stark broadening. In general, bound-bound Stark widths are determined using the semi-empirical model of Griem [21]. For dense plasmas, K-shell line Stark widths are based on fits to MERL [22] calculations. These include all He- and H-like resonance lines for Z = 10 – 20 [23], and inner-shell *1s-2p* transitions for Ne-like through Li-like lines [24]. The former are widely used to diagnose densities in inertial fusion implosion experiments, while the latter are important in simulating inner-shell absorption spectra for dense plasmas at relatively low temperatures.

Continuum lowering effects are modeled using an occupation probability model [25], supplemented by the ionization potential depression formalism of More [26], as described in Ref. [10].

Atomic cross section and energy level data are generated using the ATBASE suite of codes [27]. Major features of the ATBASE database are discussed in Appendix A.

Graphical Output

SPECT3D can be run interactively, in which case an imaging progress monitor is shown, or in batch mode. In either case, spectral and atomic level population data are written to files. Data written to these files do not include any instrumental response effects, such as spectral resolution, time-gating, or spatial smoothing. Simulation results are displayed using the SPECT3D VISUALIZER application, at which time various instrumental effects can be applied.

Using the VISUALIZER application, a wide variety of spectral diagnostics can be viewed, including time-resolved spectral lineouts, images of streaked spectra, time-integrated/time-gated spectra, and spectra that are spatially resolved in one dimension. Simulated images are frequency-integrated and can include the effects of filters. Time-integration and time-gating effects, as well as spatial smoothing can be applied to images. In accounting for spatial and spectral instrumental resolution effects, the SPECT3D results are convolved with Gaussian profiles having a user-specified width.

In generating drilldown plots, VISUALIZER interactively accesses the physics algorithms used by SPECT3D and the atomic level populations stored from SPECT3D runs. Drilldown plots – *i.e.*, lineouts of plasma properties and radiation field characteristics along a specified line-of-sight from the detector through the plasma – can be generated to view a wide variety of properties, including plasma temperatures, densities, ionization distributions, and atomic level populations; atomic rates and rate coefficients that affect a particular atomic level at a particular volume element along the LOS; and radiative properties such as specific intensity and optical depth at specified photon energies. Example results from SPECT3D and VISUALIZER are shown below.

The graphics library used supports displays of line plots, 2-D color contours, and 3-D surface plots. In addition, results from different SPECT3D simulations can be easily compared using the drag-and-drop capability in the VISUALIZER application. Plots generated by SPECT3D can also be copied directly into common Microsoft applications such as MS Word and Powerpoint.

User Interface

While SPECT3D has been designed for ease of use, it also provides for a wide range of options, thereby allowing users with a broad range of experience in plasma radiation and atomic physics to utilize the code effectively. Problem setup involves cycling through a series of user interface (UI) panels. Online help for individual panels can be accessed directly through panel-specific Help buttons. In addition, setup panels readily launch related applications for setting up customized atomic models for running non-LTE kinetics simulations.

Platforms

SPECT3D has been developed using cross-platform C++ user interface software, and utilizes the OpenGL graphics application framework, which allows SPECT3D to run on a wide variety of platforms. SPECT3D currently runs on Windows, Mac OSX, and Linux platforms. A parallel version of SPECT3D has been developed for Linux clusters to support large-scale calculations. This version decomposes the frequency grid used in computing both photoabsorption rates and emergent spectra, and is supported for all plasma geometries. To support post-processing of large-scale 3-D datasets, parallelization of the spatial grid (domain decomposition) is under development.

EXAMPLE APPLICATIONS

To illustrate some of the uses of SPECT3D, we present example results from simulations of: (1) a radiatively-driven inertial fusion capsule implosion experiment; (2) photo-pumping effects in a z-pinch dynamic hohlraum experiment; and (3) backlit imaging of a radiation-driven jet. These simulations are based on experiments performed at major laser and z-pinch facilities, and results are selected to show a variety of types of SPECT3D simulation output. Other examples of the use of SPECT3D have been presented elsewhere, including the analysis of monochromatic spherical crystal imaging of the early evolution of z-pinch wire arrays [28], visible and infrared spectra from hypervelocity impact flash experiments [29], and backlit imaging of polar direct drive imploding capsules [30].

Figures 3 to 5 show spectra, monochromatic radial intensity profiles, and drilldown plots from simulations of indirect drive capsule implosion experiments [31-33]. In these experiments, performed at the OMEGA laser facility, a hohlraum radiation field with a radiation temperature of ~ 190 eV was used to implode a spherical 220 μm-diameter, 35 μm-thick CH capsule with an Ar-doped DD fill gas. A 4 μm-thick PVA (C_2H_4O) layer was embedded in the CH to help contain the gas. The implosion was simulated using a 1-D radiation-hydrodynamics code, HELIOS-CR, that includes inline non-LTE atomic kinetics modeling [10]. Figure 3 shows SPECT3D results for time-resolved, space-integrated (*i.e.*, integrated over the 2-D detector plane) spectra of the Ar K-shell emission. The simulated atomic level populations and

resulting spectra were computed using full non-LTE modeling in which multi-angle radiative transfer modeling was used in computing photoionization and photoexcitation rates. The simulated spectra shown assume an instrumental resolution of $\lambda/\Delta\lambda = 800$. The He-like and H-like resonance lines are clearly seen, along with prominent emission from satellites to the He-α ($1s2p \rightarrow 1s^2$) and Ly-α ($2p \rightarrow 1s$) lines. The peak emission at 1.7 ns corresponds to the time of peak compression in the RH simulation. At later times (t = 1.8 ns), the emission from the H-like lines is seen to drop much faster than the emission from the He-like lines.

Figure 4 shows radial intensity profiles (*i.e.*, the intensity in the detector plane along a radial) from simulated monochromatic images of Ar He-β ($1s3p \rightarrow 1s^2$) and Ly-β ($3p \rightarrow 1s$) emission lines at simulation times of 1.6, 1.7, and 1.8 ns. Monochromatic imaging of these lines has been shown to be useful in studying the core plasma temperature and density distributions [31,34]. The radial profiles are obtained by generating images in narrow bands (ΔE = 70 eV) centered about the He-β and Ly-β lines. The results show that: the intensity is highest at the time of peak compression (1.7 ns); the He-β profile is relatively flat throughout out to a larger radial distance; and the Ly-β intensity decreases much more rapidly after the time of peak compression.

Drilldown plots of plasma properties and radiation field characteristics computed using SPECT3D at a simulation time of 1.7 ns are shown in Figure 5. Drilldown plots are a powerful tool in assessing where the radiation seen by a detector is emitted and absorbed along a line-of-sight as it propagates through the plasma towards the detector. The results in Fig. 5 correspond to a LOS that goes directly through the center of the capsule. In each case, quantities are plotted as a function of "depth," which in this case is defined by the integrated areal density ($\int \rho\, dz$), as measured from the plasma boundary on the detector side of the plasma (this representation is often useful in more clearly identifying the effects of different materials). The electron temperature and material mass densities for the Ar-doped DD (ArDD), CH, and PVA are shown on the left plots. Note that the compressed ArDD resides at a depth of between 24 and 40 mg/cm^2. It is this region where the temperature is highest, and most of the x-ray emission originates. The plots on the right show the specific intensity along the LOS (in the direction toward the detector) and the optical depth measured from the detector side of the plasma boundary at photon energies

corresponding to the centers of the Ar He-α, He-β, He-γ, and Ly-α emission lines. Looking at the He-α line (solid curves in the right plots), the total line center optical depth integrated along the LOS through the center of the compressed capsule is ~ 30. The compressed ablator (CH+PVA) on the detector side of the LOS has an optical depth of 0.9. The specific intensity *directed toward the detector* at the rear side of the plasma (*i.e.*, the right edge of the plot) is zero, as the boundary condition is zero unless there is a backlighter. Moving from right to left in the plot (*i.e.*, from the back of the plasma towards the detector), the specific intensity remains low until the ArDD is reached. The He-α intensity then increases rapidly and peaks at a point near where the electron temperature is highest. The intensity then decreases as it nears the CH-ArDD interface. This is due to the fact that the He-α radiation is optically thick in the ArDD region and that the source function (see Eq. (3)) drops because of the lower temperatures near the boundary. In the CH ($\int \rho \, dz$ < 24 mg/cm^2), the He-α intensity continues to drop due to the bound-free opacity of the CH and PVA. For the LOS and simulation time considered here, the line center He-α intensity drops by approximately a factor of 2 between the CH-ArDD boundary and the plasma grid boundary. By comparison, the specific intensities of the He-β and He-γ lines increase monotonically within the ArDD region. This is because the optical depth at the center of these lines is low ($\lesssim$ a few tenths).

Figure 6 shows examples of SPECT3D space-resolved spectra computed to study the effects of photo-pumping in z-pinch dynamic hohlraum experiments [35,36]. In these experiments, a strong high-temperature shock propagates radially inward through a low-density Si-doped CH foam. Space-resolved Si K-shell spectra are obtained by measuring the emission through a slit over the top of the cylindrical foam. The spectra are integrated over the width of the slit, and resolved over the length of the slit. Fig. 6 shows space-resolved spectra computed by post-processing the results from 1-D HELIOS-CR calculations using SPECT3D at a time when the shock is at a radius of 0.27 cm. The shock lies just in front of a tungsten plasma moving radially inward. Results are shown for two cases: one where the atomic level populations are computed assuming LTE (top image), the other in which non-LTE calculations were performed which take into account photo-pumping effects from radiation emitted by the high-temperature shock (bottom image). In each case, an instrumental broadening of $\lambda/\Delta\lambda = 300$ is applied to the simulated

spectra. In the LTE case, it is seen that very little Si K-shell emission occurs in the Si-doped CH at radii interior to the shock, while significant emission originating from the shock itself is clearly seen (at a position of ± 0.27 cm). This is because the electron temperature ahead of the shock is much lower than the shock temperature. In the non-LTE simulation, photoionization and photoexcitation of the Si dopant in the foam ahead of the shock occurs. That is, radiation emitted by the shock ionizes and excites the Si, strongly affecting the spectral emission seen by a spectrometer located above the top of the foam.

As a final example, Figure 7 shows a SPECT3D simulation of a backlit image for a radiation-driven jet experiment. These results are obtained by post-processing the results of ALEGRA simulations with 2-D cylindrical *r*-*z* geometry [37]. In this simulation, a cylindrical Al pin is radiatively heated and expands into a CH layer. The evolution of the expanding Al is tracked by backlighting the plasma with intense Fe He-α emission at 6.7 keV. The image on the left in Fig. 7 shows a 3-D rendering of the detector-target orientation, which shows the intersection of the target plasma and the detector viewing volume. Here, the plasma conditions from the RH simulation for this 2-D *r*-*z* geometry simulation are shown in intersection planes showing color contours of the temperature. This ability to examine a 3-D view of the detector-target orientation is very useful in checking on whether the detector position and image plane parameters are set up appropriately prior to the simulation. The image at the right shows the simulated backlit image, where the relatively high intensity regions correspond to backlighter photons that propagate through the CH and miss the Al. The lower intensities along the axis of symmetry ($X_{Det} = 0$) are due to bound-free absorption of the backlighter by the Al. In designing backlighter experiments of this type, SPECT3D is a useful tool in determining contrast levels (*i.e.*, amount of attenuation at backlighter wavelengths).

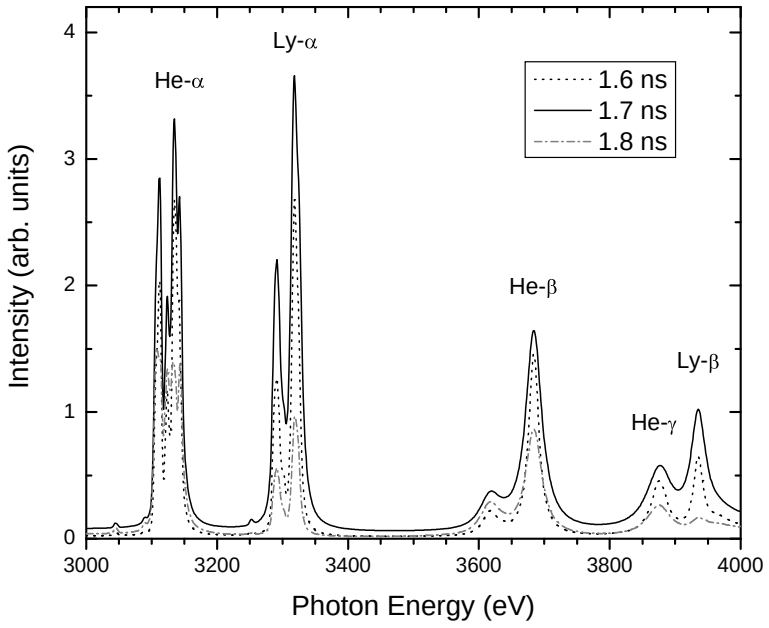

Figure 3. Time-resolved, space-integrated Ar K-shell emission spectra obtained by post-processing a radiation-hydrodynamics simulation of an Ar-doped capsule implosion. Spectra are shown at simulation times of 1.6, 1.7, and 1.8 ns, and assume an instrumental resolution of $\lambda/\Delta\lambda = 800$.

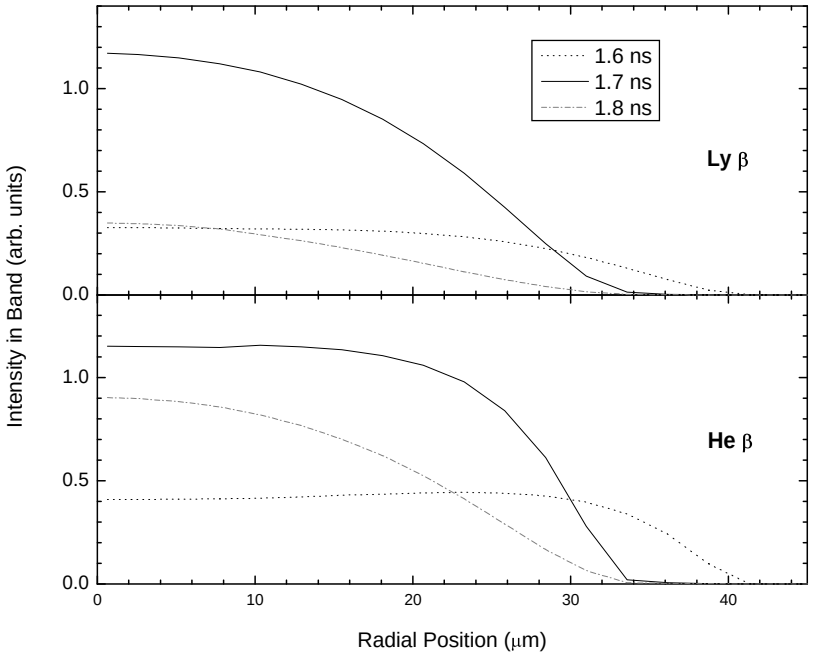

Figure 4. Time-resolved radial emission profiles from narrow-band images of the Ar He-β and Ly-β lines at simulation times of 1.6, 1.7, and 1.8 ns.

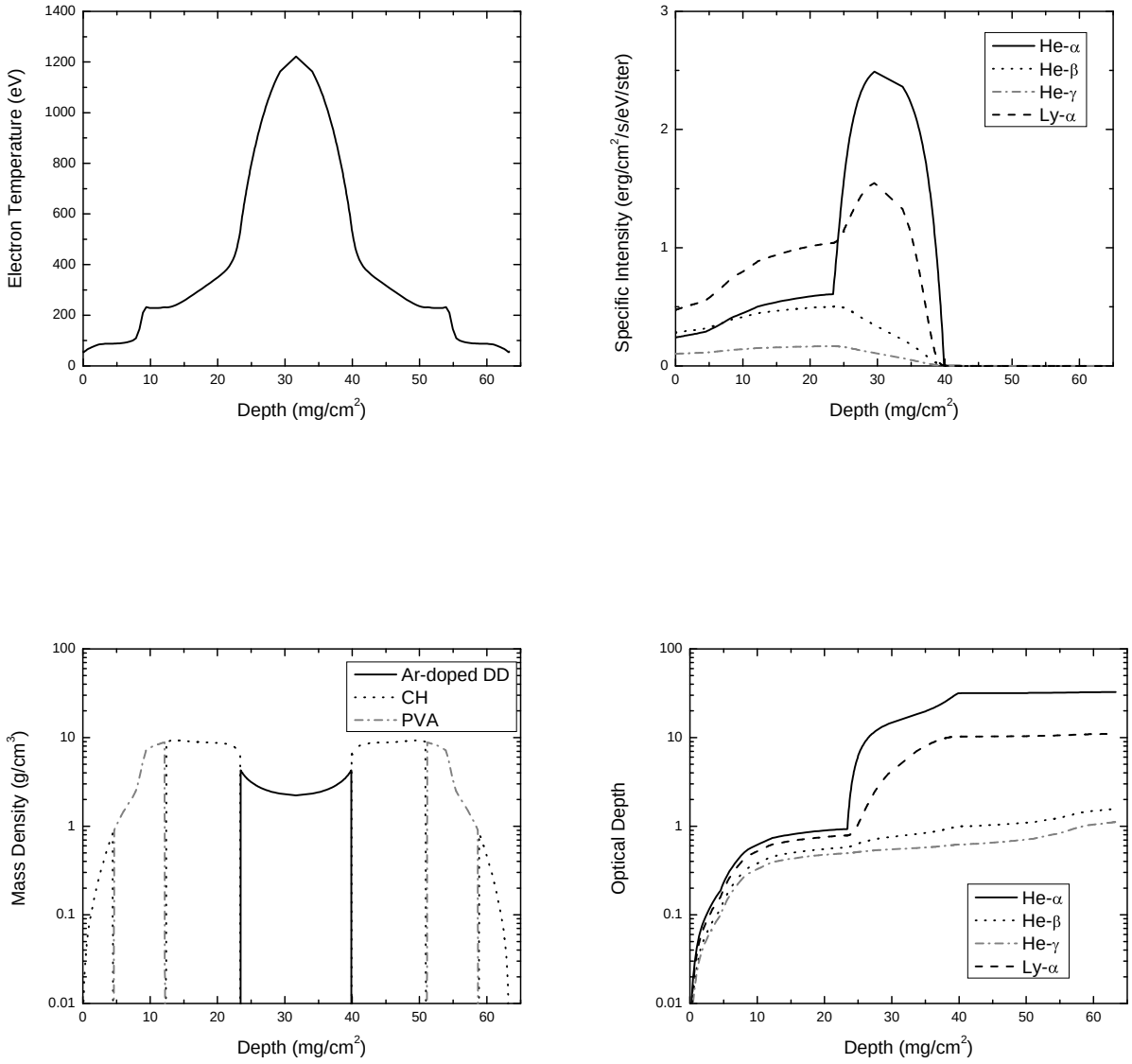

Figure 5. Drilldown plots showing depth-dependence of plasma properties and radiation field characteristics along a line-of-sight (LOS) that extends from the detector through the center of the compressed capsule. The depth is defined in terms of the areal density ($\int \rho \, dz$) integrated along the line of sight. Upper left: Electron temperature. Lower left: Material densities for Ar-doped DD, CH, and PVA. Upper right: Specific intensity along the LOS in the direction towards the detector at line center wavelengths of the Ar He-α, He-β, He-γ, Ly-α lines. Lower right: Optical depth integrated from the detector-side edge of the plasma at the line center wavelengths of the Ar He-α, He-β, He-γ, Ly-α lines.

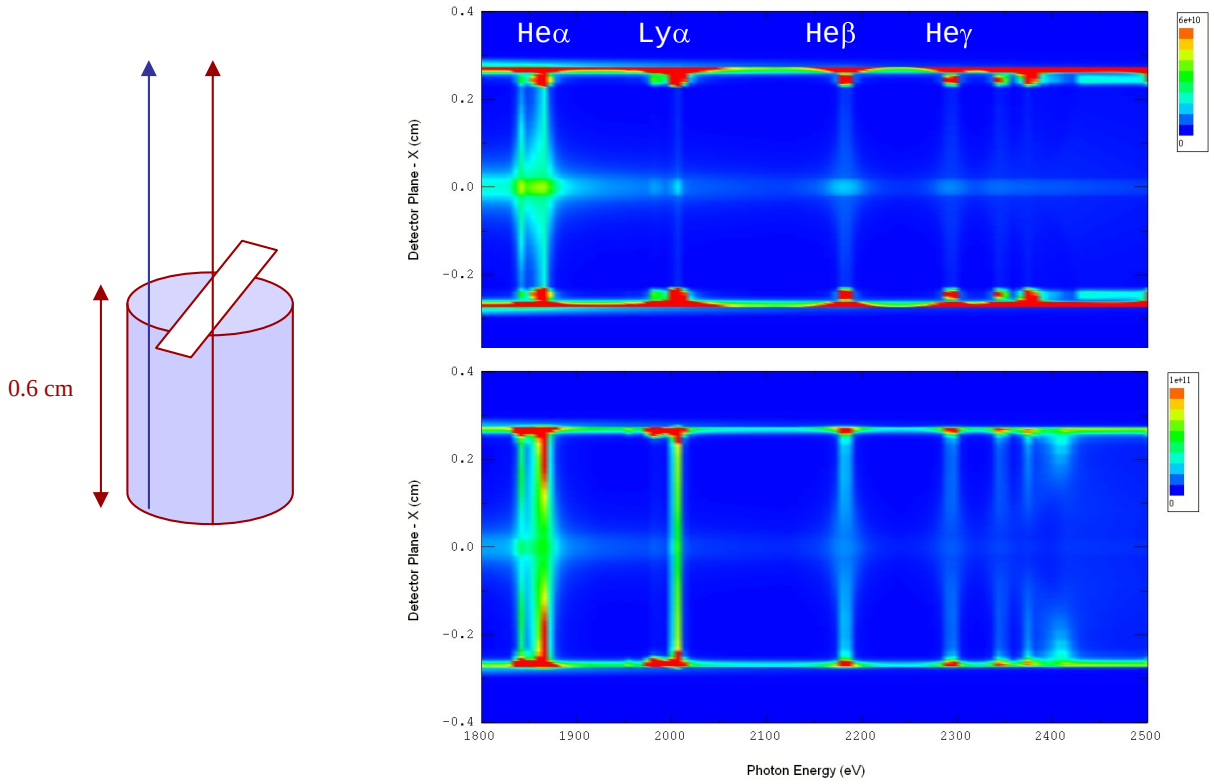

Figure 6. Left: Schematic illustration of plasma and detector setup in ZPDH experiment. Right: Simulated 1-D space-resolved spectra (*i.e.*, integrated over the slit width) of Si K-shell emission from a Si-doped CH foam. Top: spectrum computed under the assumption of LTE. Bottom: full non-LTE simulation. The strong emission across the spectra at positions of $x = \pm$ 0.25 cm corresponds to a thin high temperature shock region. A spectral resolution of $\lambda/\Delta\lambda = 300$ is applied to simulation results.

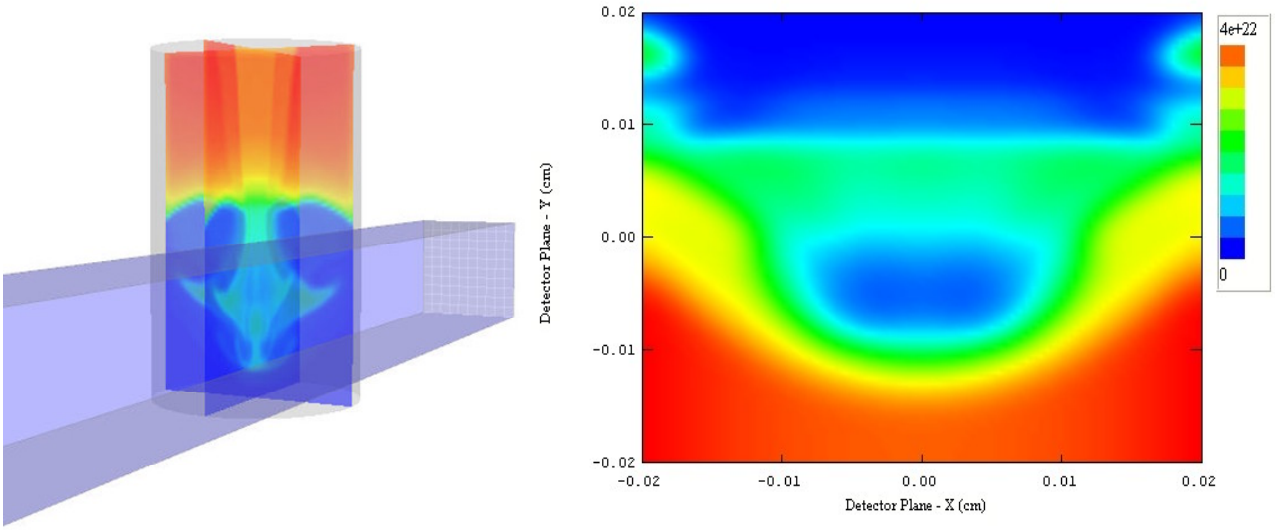

Figure 7. Left: 3-D image showing the detector-target orientation for radiation-driven jet simulation. Right: Backlit image radiation-driven Al jet expanding into CH for a $h\nu$ = 6.7 keV backlighter.

SUMMARY

SPECT3D is an easy-to-use multi-dimensional collisional-radiative code that generates diagnostic signatures (*e.g.*, images, spectra), based on radiation-hydrodynamics and PIC code output, that can be directly compared with experimental measurements. It is currently being used to post-process output from several state-of-the-art RH and PIC simulation codes used in designing and analyzing HEDP experiments. It includes physics algorithms for accurately simulating the radiative properties of LTE and non-LTE plasmas, including the effects of energetic particles that are generated in intense short-pulse laser experiments. Comparisons with experimental measurements allow one to assess the reliability of RH or PIC code simulation predictions. SPECT3D can also be used to predict signal levels (*e.g.*, absolute fluxes and line intensities) for the purpose of designing experiments and utilizing diagnostic instruments effectively. Because of its ease of use and supporting graphics, it is also a useful tool for training graduate and undergraduate students in the area of plasma and radiation physics.

APPENDIX A

The atomic database used by SPECT3D includes energy level and transition data for all ions of a given element. Atomic cross section data are generated using the ATBASE suite of codes [27]. This suite of codes is composed of a collection of publicly available codes [38-41] and a series of codes developed and refined by the authors [42,43]. Energy level data include energies, statistical weights, *j* values, and mean square orbital radii. Transition data include electron-impact ionization and excitation cross sections and rate coefficients, oscillator strengths, photoionization cross sections and radiative recombination rate coefficients, autoionization rates and dielectronic recombination rate coefficients, and proton-impact ionization and excitation cross sections.

Energy levels, photoionization cross sections, oscillator strengths, autoionization rates, and electron collision cross sections are calculated using a configuration interaction method with relativistic Hartree-Fock wavefunctions under an intermediate-coupling scheme. Oscillator strengths are calculated for all electric dipole (E1), electric quadrupole (E2), and magnetic dipole (M1) transitions. An extensive configuration list for each isoelectronic sequence has been carefully setup and tested to support modeling for a wide range of plasma spectral properties.

Collisional coupling between states is complete – *i.e.,* all thermal (non-autoionizing) and autoionizing states are collisionally coupled – with electron-impact collisional excitation and ionization cross sections computed using a distorted wave (DW) model [44]. The DW calculations include exchange effects, and therefore provide reliable cross sections for both spin-conserved ($\Delta S=0$) and spin change ($\Delta S>0$) transitions.

Using a relativistic generalized oscillator strength formalism [45,46], we have extended our electron-impact excitation and ionization cross section calculations to high energies utilizing a relativistic first order Born approximation framework. For excitation processes, relativistic Dirac-Fock wavefunctions are used for both initial and final states. For ionization processes, the high energy electron and the electron ejected from the atom are treated differently. The high energy electron is described by plane-wave solutions of the Dirac equation. The atomic electrons and ejected electron are treated

relativistically as moving in a Dirac-Fock potential. This treatment is reasonable because for incident electron energies that are much greater than the binding energies of bound electrons, the interference effects between the scattered and the ejected electron are very small because the energy lost to the ejected electron is of the order of the binding energy. The first order Born approximation is used to treat the interaction of the high energy and atomic electrons. By using Dirac-Fock wavefunctions and a relativistic calculation of the matrix elements, our calculation represents a significant improvement over many previous relativistic calculations which have been carried out using non-relativistic-based values of the matrix elements based either on a Coulomb potential or on the connection with radiative oscillator strengths and photoionization cross sections.

Dielectronic recombination processes involving autoionization states of Ne-like ions and higher can be treated explicitly, with electron capture rates determined from detailed balance with their corresponding autoionization rates. For lower ionization stages, autoionization states are not explicitly included in the atomic model, and effective dielectronic recombination rates are utilized.

Calculations for ion impact ionization cross sections are made using a plane-wave Born approximation (PWBA) model with corrections for polarization and binding effects, coulomb deflection, and relativistic effects [47]. Calculated cross sections for both low-Z and high-Z targets using this model have been found to be in good agreement with experimental data [48,49].

REFERENCES

[1] Lindl J. Development of the indirect-drive approach to inertial confinement fusion and the target physics basis for ignition and gain. Phys. Plasmas 1995; 2: 3933-4024.

[2] Bailey JE, et al. Dynamic hohlraum radiation hydrodynamics. Phys. Plasmas 2006; 13: 056301,1-9.

[3] Slutz S, et al. Dynamic hohlraum driven inertial fusion capsules. Phys. Plasmas 2003; 10: 1875-1882.

[4] Welch DR, et al. Integrated simulation of the generation and transport of proton beams from laser-target interaction. Phys. Plasmas 2006; 13: 063105, 1-12.

[5] Tabak M, et al. Review of progress in fast ignition. Phys. Plasmas 2005; 12: 057305, 1-8.

[6] Bakshi V. EUV Sources for Lithography. Bellingham WA: SPIE Press, 2006.

[7] Brunner, TA, Mehlhorn, TA. User's guide to radiation transport in ALEGRA-HEDP, Technical Report SAND-2004-5799, Sandia National Laboratories, Albuquerque, NM, November, 2004.

[8] Radha PB, et al. Two-dimensional simulations of plastic-shell, direct-drive implosions on OMEGA. Phys. Plasmas 2005; 12: 032702, 1-18.

[9] McGlaun JM, Thompson SL. CTH: A three-dimensional shock wave physics code. Intl J Impact Engr 1990; 10: 351-360.

[10] MacFarlane JJ, Golovkin IE, Woodruff PR. HELIOS-CR – A 1-D radiation-magnetohydrodynamics code with inline atomic kinetics modeling. J Quant Spectrosc Radiat Transfer 2006; 99: 381-397.

[11] Welch DR, Rose DV, Oliver BV, Clark RE. Ballistic neutralized chamber transport of intense heavy ion beams. Nucl. Instrum. & Methods Phys. Res. A 2001; 464: 134.

[12] Hughes TP, Yu SS, Clark RE. Three-dimensional calculations for 4-kA, 3.5 MV, 2-nanosecond injector with asymmetric power feed. Phys. Rev. ST-AB 1991; 2: 110401.

[13] MacFarlane JJ, et al. Simulation of the ionization dynamics of aluminum irradiated by intense short-pulse lasers. Proc. Inertial Fusion and Science Applications 2003. La Grange Park IL: Amer. Nucl. Soc., 2004.

[14] See Appendix of Ref. 10.

[15] Mihalas D. Stellar Atmospheres. New York: WH Freeman and Co, 1978.

[16] McQuarrie DA. Statistical Mechanics. New York: Harper & Row, 1976.

[17] Apruzese JP. An analytic Voigt profile escape probability approximation. J Quant Spectrosc Radiat Transfer 1985; 34: 447-452.

[18] Van Nort M, Hubeny I, Lanz T. Multidimensional non-LTE radiative transfer. I. A universal two-dimensional short-characteristics scheme for Cartesian, spherical, and cylindrical coordinate systems. Astrophys J 2002; 568: 1066-1094.

[19] Olson GL, Kunasz PB. Short characteristic solution of the non-LTE line transfer problem by operator perturbation – I. The one-dimensional slab. J Quant Spectrosc Radiat Transfer 1987; 38: 325-336.

[20] Chung H-K, Chen MH, Morgan WL, Ralchenko Y, Lee RW, High Energy Dens. Phys. 2005; 1: 3-12.

[21] Griem HR. Semiempirical formulas for the electron-impact widths and shifts of isolated ion lines in plasmas. Phys. Rev. 1968; 165: 258-266.

[22] Woltz LA, Hooper CF. Calculation of spectral line profiles of multielectron emitters in plasmas. Phys Rev A 1988; 38: 4766-4771.

[23] Haynes DA. Private communication. 2001.

[24] Mancini RC. Private communication. 2006.

[25] Hummer DG, Mihalas D. The equation of state for stellar envelopes. I. – an occupation probability formalism for the truncation of internal partition functions. Astrophys J 1988; 331: 794-814.

[26] More RM. Applied Atomic Collision Physics, vol. 2. New York: Academic Press, 1982.

[27] Wang P. Computation and application of atomic data for inertial confinement fusion plasmas. PhD dissertation, Dept of Nuclear Engineering and Engineering Physics, Univ of Wisconsin, Madison, WI, 1991.

[28] Sinars DB, et al. Measurements and simulations of the ablation stage of wire arrays with different initial wire sizes. Phys. Plasmas 2006; 13: 042704, 1-13.

[29] Lawrence J. Spectral measurements of hypervelocity impact flash. 9th Hypervelocity Impact Symposium, Lake Tahoe CA, 2005.

[30] Craxton RS, et al. Polar direct drive: Proof-of-principal experiments on OMEGA and prospects for ignition on the National Ignition Facility. Phys. Plasmas 2005; 12: 056304, 1-8.

[31] Welser LA, et al. Analysis of the spatial structure of inertial confinement fusion implosion cores at OMEGA. J Quant Spectrosc Radiat Transfer 2003; 81: 487-497.

[32] Welser LA, et al. Processing of multi-monochromatic x-ray images from indirect drive implosions at OMEGA. Rev. Sci. Instrum. 2003; 74: 1951-1953.

[33] MacFarlane JJ, et al. Dopant radiative cooling effects in indirect-drive Ar-doped capsule implosion experiments. Phys Rev E 2005; 72: 066403, 1-14.

[34] Golovkin IE, et al. Spectroscopic determination of dynamic plasma gradients in implosion cores. Phys. Rev. Lett. 2002; 88: 045002, 1-4.

[35] Bailey JE, et al. Time- and space-resolved spectroscopy of dynamic hohlraum interiors. High Energy Density Phys 2005; 1: 21-30.

[36] MacFarlane JJ, et al. Modeling of dopant spectral emission in z-pinch dynamic hohlraum experiments. 47th APS Division of Plasma Physics Meeting, Denver CO, 2005.

[37] Keiter PA, et al. Hydrodynamic experiments that simulate jets in supernova explosions. American Physical Soc Meeting, Philadelphia PA, 2003.

[38] Fischer CF. A general multi-configuration Hartree-Fock program. Comp Phys Comm 1978; 14: 145-153.

[39] Fischer CF, Liu B. A program to generate configuration-state lists. Comp Phys Comm 1990; 64: 406-416.

[40] Fischer CF. The MCHF atomic-structure package. Comp Phys Comm 2000; 128: 635-636.

[41] Abdallah J, Clark REH, Cowan RD. Theoretical atomic physics code development I. CATS: Cowan atomic structure code. Los Alamos Laboratory Report LA-11436-M, Los Alamos NM, 1988.

[42] Wang P, MacFarlane JJ, Moses GA. Relativistic-configuration-interaction calculations of Kα satellite properties for aluminum plasmas created by intense proton beams. Phys Rev E 1993; 48: 3934-3942.

[43] Wang P, MacFarlane JJ, Moses GA. Thermal ionization effects on inner-shell line emission for Au targets heated by intense light ion beams. Rev Sci Instrum 1992; 63: 5059-5061.

[44] Sobelman II, et al. Excitation of Atoms and Broadening of Spectral Lines. New York: Springer-Verlag, 1981.

[45] Inokuti M. Inelastic collisions of fast charged particles with atoms and molecules – the Bethe theory revisited. Rev Mod Phys 1971; 43: 297-347.

[46] Bretagne J, Callede G, Legentil M, Peuch V. Relativistic electron-beam-produced plasmas. I: Collision cross sections and loss function in argon. J Phys D 1986; 19: 761-777.

[47] Brandt W, Lapicki G. L-shell Coulomb ionization by heavy charged particles. Phys Rev A 1979; 20: 465-480.

[48] Datz S, et al. Cross sections for L-subshell ionization in Au by the collision of protons and helium ions. Phys Rev A 1974; 9: 192-196.

[49] Khan JM, Potter DL, Worley RD. Sutdies in x-ray production by proton bombardment of C, Mg, Al, Nd, Sm, Gd, Tb, Dy, and Ho. Phys Rev A 1965; 139: 1735-1746.